Barcheck, C.G., Schwartz, S.Y., and Tulaczyk, S., 2020, Icequake streaks linked to potential megascale glacial lineations beneath an Antarctic ice stream: Geology, v. 48, https://doi.org/10.1130/G46626.1

Icequake detection method: Additional Details

Basal icequakes are seismic events happening at or near the ice-bed interface. These events are small amplitude, typically have clear P and S waves (Fig 1C) and can only be detected within a few km of the seismic source. Beneath our seismic network on the Whillans Ice Plain (WIP), basal icequakes typically occur only during ice plain wide unstable slip events, when ice sliding is fastest. During an unstable slip event, hundreds to thousands of basal icequakes can occur within ~30 minutes, with waveforms often overlapping in time and making traditional detection and association methods challenging. We use an S-wave backprojection technique to detect and preliminarily locate basal icequakes. We focus on horizontal component S-wave detection only because (1) P-waves attenuate at much smaller epicentral distances than S-waves (~1-2 km), and (2) P-wave duration is extremely short compared with S-wave duration, making them inadequate for backprojection.

Nine and eight short period surface seismometers were operated at the location shown in Fig 1D in January-February 2014 and January 2015, respectively, and we analyze data for 21 days (30 unstable slip events) in 2014, and 14 days (18 unstable slip events) in 2015. Instruments were arranged in a small network (triangles in Fig 2A) near the central nucleation area of WIP unstable slip events (Figure 1D) (Pratt et al., 2014). Instruments are 1 km apart or less, allowing small amplitude basal icequake seismic waves to be recorded by multiple instruments. Sercel L22 short period seismometers were leveled and directly buried in the snow ~1 meter below the snow surface in January 2014, and exhumed, re-leveled, and re-buried in January 2015. Three-component seismic data is collected at either 1000 Hz or 250 Hz. All processing is done using the ObsPy seismic data processing package (Krischer et al., 2015).

Seismometer locations are offset between 2014 and 2015 due to downstream ice motion of ~270 m. We determine seismometer locations each year using a handheld GPS unit, with measurements made on different days. To correct for differential downstream advection of seismic sites, all sites are extrapolated upstream to a common time for each year using

displacement recorded by a local GPS site (circles in Fig 2A). We then assume seismometer locations to be fixed, despite continuous ice displacement (~19 m in 2014, ~13 m in 2015), because displacement during the experiment is less than half of the 50 m grid point spacing. Some apparent smearing of seismicity into the next upstream grid point is possible but will not affect overall seismicity patterns.

First, we select high quality horizontal component data from 15 minutes before through 60 minutes after the GPS-determined start of each unstable slip event. We then apply a 1-125Hz band-pass filter and decimate data to 250 Hz (black data, Figure S1). We next convert the decimated data to short term average over long term average (STA/LTA) data streams (light grey data, Figure S1) using windows of 0.02 and 0.2 seconds, which were determined to maximize S wave detection and minimize noise detection. The STA/LTA data are further modified by setting all values below 3.2 equal to zero (colored data, Figure S1). These steps isolate local S-wave arrivals of appropriate duration for basal icequakes (Fig S1).

We then generate a grid of potential icequake source locations beneath the seismic network at the base of 690 m thick ice, with ice depth determined from the CReSIS radar (CReSIS, 2014). Grid point spacing is 50 m, and only gridpoints within 1200 m of a seismometer (in map view) are considered, to ensure that only grid points within a reasonable distance of the network can have basal icequake detections. Grid points are at the center of pixels shown in Figs 2A, S3, and S4, and absolute grid point locations do not change between years.

We calculate S-wave travel times from all grid points to all seismometers using the ObsPy *taup* module (Krisher et al., 2015) and the ice velocity model shown in Fig S2. This velocity model is determined using the temperature-velocity relationship of Kohnen (1974) applied to a vertical ice temperature profile from a borehole above nearby Subglacial Lake Whillans (SLW) (Fisher et al., 2015). The near-surface S-wave velocity at SLW is estimated from a P-wave velocity profile generated by a seismic refraction survey conducted over SLW in 2010/11 (Horgan, WISSARD internal report, 2011) and assuming a Poisson solid. We then vertically scale the SLW velocity model by the relative ice thicknesses of 690 m at the seismic network (CReSIS, 2014) and 800m at SLW (Tulaczyk et al., 2014). The resulting S-wave velocity profile is shown in Fig S2.

Next, thresholded STA/LTA data are migrated back in time by the travel time for each grid point – seismometer pair, resulting in a set of migrated STA/LTA data streams for each grid point, illustrated in Figure S1B. Prior to stacking, the migrated STA/LTA data are weighted according to the horizontal distance between each seismometer and grid point. This step is done to reduce the potential mis-association of seismic wave arrivals from disparate parts of the seismic network. STA/LTA streams are weighted by the seismometer-grid point horizontal distance D_{ij} in the following way:

$$W_{ij} = \begin{cases} 1, D_{ij} < d_1 \\ \frac{1}{2} cos\,[\frac{\pi}{d_0 - d_1}(D_{ij} - d_1) + 1], d_0 < D_{ij} < d_1 \\ 0, D_{ij} > d_0 \end{cases}$$

where W_{ij} is the weighting factor for arrivals from seismometer i to grid point j, d_1 is the distance inside which all weights are 1, and d_0 is the distance beyond which all weights are set to zero. We use d_1 = 750 m, and d_0 = 3250 m; both are chosen to maximize detections and minimize mis-detections. This weighting scheme ensures that arrivals at seismometers far from a grid point cannot contribute heavily to STA/LTA stacks.

Next, thresholded and migrated STA/LTA data at each grid point are stacked. After this step, any peaks in stacked power are probable detections. To determine a detection threshold, the stacked STA/LTA data for all grid points are subset into 20 second (2014) or 30 second (2015) windows. Within each window, data are further windowed into 0.24 second sub-windows, and two vectors are created for each grid point: the maximum value of the stack in each 0.24 second sub-window (s_{max}), and the power of the stack (sum of squared amplitude) in each 0.24 second sub-window (s_{pow}). An example "beam" of back-projected power determined for a single 0.24 second sub-window is shown in Fig S3. Two detection thresholds are then set for each 20 or 30 second window:

$thresh_1$ = mean (s_{max}) + 6 * standard deviation (s_{max}), and

$thresh_2$ = mean (s_{pow}) + 6 * standard deviation (s_{pow}).

Any 0.24 second window with maximum value or power above the corresponding threshold is marked as a detection, provided that 7 or more S-waves contribute to the detection (minimum 4

seismic sites if both horizontal channels are operating). These thresholds keep only the highest quality detections, meaning that many overlapping or smaller icequakes are likely ignored.

The tan area surrounding the seismic network in Figures 2 and S4 indicates grid points that are too far away from the network for the network to be sensitive to a basal icequake happening in that location. The tan area shows grid points that are more than 1200 m from a seismometer, have fewer than 7 possible S wave arrivals total, or fewer than 7 possible arrivals from any seismometer with $W_{ij} > 0.5$. Thus, the white and grey region inside the tan area represents the area of the ice stream bed to which the seismic network is sensitive, though sensitivity does decrease towards the edges.

Basal icequakes are detected using this backprojection method on a total of 30 unstable slip events in Jan-Feb 2014 and 18 unstable slip events in Jan 2015. In a typical individual unstable slip event, only a few tens to a few hundreds of basal icequakes are detected, and only at a handful of grid points (Figure S4). The streaked seismic pattern does not emerge until cumulative seismicity from many unstable slip events is analyzed. Additionally, the seismically active grid points from one unstable slip event are rarely the same active locations in the next unstable slip. This is illustrated in Figure S4, showing two consecutive unstable slip events in January 2014 with very different seismicity rates and locations.

Radar resolution

The range resolution r for two closely-spaced englacial reflectors is $r = \frac{k_t c}{2B\sqrt{3.15}}$, where k_t is a window widening factor, c is the speed of light in a vacuum, B is the bandwidth of the radar system, and 3.15 is the approximate dielectric of ice (CReSIS, 2016). For the 2013_Antarctica_Basler dataset used in this study, k_t is 1.53, and B is 250 MHz, giving a range resolution r of 0.52 m, meaning two reflections that are ~0.5 m apart can be distinguished.

For an isolated reflector, such as the ice stream bed often is, the range resolution improves depending of the signal to noise ratio (*SNR*) of the reflector and the surrounding noise environment: $r = \frac{k_t c}{2B\sqrt{3.15}\sqrt{2*SNR}}$ (CReSIS, 2016). Therefore, even for a low *SNR* of 2, the range resolution of a single reflector such as the ice stream bed decreases to 0.26 m. Thus, the range

resolution of the ice stream bed is never more than ~0.5m, and the few m amplitude bumps shown in Fig 2C are observable given the resolution of the radar system.

Additional radar evidence of MSGL beneath the Whillans Ice Plain

In addition to the short segment of radar shown in Figure 2, we looked for evidence of MSGL or other bedforms in three longer sections of well-oriented radar lines collected in the vicinity of our study area in December-January 2013-2014 (CReSIS, 2014). The locations of these three lines are shown in Figure S5, panel A.

Because we are interested in basal topography with across-flow wavelength comparable to MSGL, we rotate the polar stereographic X and Y positions for each radar datapoint into an along- and across-flow coordinate system using an ice-flow vector (thin maroon line, Fig S5 A) determined from on-ice GPS installed at the seismic network (magenta dot, Fig S5 A). Ice bottom elevation as a function of across-flow coordinate (thick maroon line, Fig S5) is plotted as the lower lines in Fig S5, panels B, C, and D. After projection, radar datapoint spacing is irregular, so we interpolate and resample the data to 20 m spacing in the across-flow direction. We then detrend and bandpass filter the ice bottom elevation data between 100 and 3000 m, shown as the upper lines in Fig S5. The across-flow position of the seismometers is additionally shown in Fig S5 panel B as blue triangles.

All three radar lines show evidence of low-amplitude bedforms, pointed out with red arrows in Fig S5. In some areas, the radar reveals a continuously undulating, wavy bed, shown for example on the right side of panel C where the bed elevation drops. These are likely bed areas with a strongly streamlined and lineated bed. Other areas exhibit relatively isolated topographic bumps of a few m amplitude, for example those pointed out in panel B. These bumps could be just the largest-amplitude bedforms, with others smaller than the radar vertical resolution, or they could be isolated MSGL on an otherwise relatively smooth bed. We generally ignore data with high-frequency bed elevation noise, assuming high-frequency noise to reflect radar depth uncertainty.

These radar observations suggest that there are abundant MSGL beneath the WIP, especially towards the right side of Fig S5, C, and D where the bed is deeper. Shallower areas of

the bed appear to have more isolated or low-amplitude undulations, suggesting that the shallower areas of the WIP are smoother in general, perhaps having fewer MSGL.

Citations:

CReSIS. 2014. 2013_Antarctica_Basler Data, Lawrence, Kansas, USA. Digital Media. http://data.cresis.ku.edu/.

CReSIS, 2016, Radar Depth Sounder Readme: ftp://data.cresis.ku.edu/data/rds/rds_readme.pdf (accessed March 2019).

Fisher, A.T., Mankoff, K.D., Tulaczyk, S.M., Tyler, S.W., Foley, N., and Team, W.S., 2015, High geothermal heat flux measured below the West Antarctic Ice Sheet: Science Advances, v. 1, doi: 10.1126/sciadv.1500093.

Horgan, H.J., 2011, Firn and ice thickness at Subglacial Lake Whillans. WISSARD internal report.

Kohnen, H., 1974, The Temperature Dependence of Seismic Waves in Ice: Journal of Glaciology, v. 13, p. 144–147.

Krischer, L., Megies, T., Barsch, R., Beyreuther, M., Lecocq, T., Caudron, C., and Wassermann, J., 2015, ObsPy: A bridge for seismology into the scientific Python ecosystem: Computational Science and Discovery, v. 8, doi: 10.1088/1749-4699/8/1/014003.

Pratt, M.J., Winberry, J.P., Wiens, D.A., Anandakrishnan, S., and Alley, R.B., 2014, Seismic and geodetic evidence for grounding-line control of Whillans Ice Stream stick-slip events: Journal of Geophysical Research: Earth Surface, v. 119, p. 333–348, doi: 10.1002/2013JF002842.

Tulaczyk, S., Mikucki, J. a., Siegfried, M.R., Priscu, J.C., Barcheck, C.G., Beem, L.H., Behar, A., Burnett, J., Christner, B.C., Fisher, A.T., Fricker, H. a., Mankoff, K.D., Powell, R.D., Rack, F., et al., 2014, WISSARD at Subglacial Lake Whillans, West Antarctica: scientific operations and initial observations: Annals of Glaciology, v. 55, p. 51–58, doi: 10.3189/2014AoG65A009.

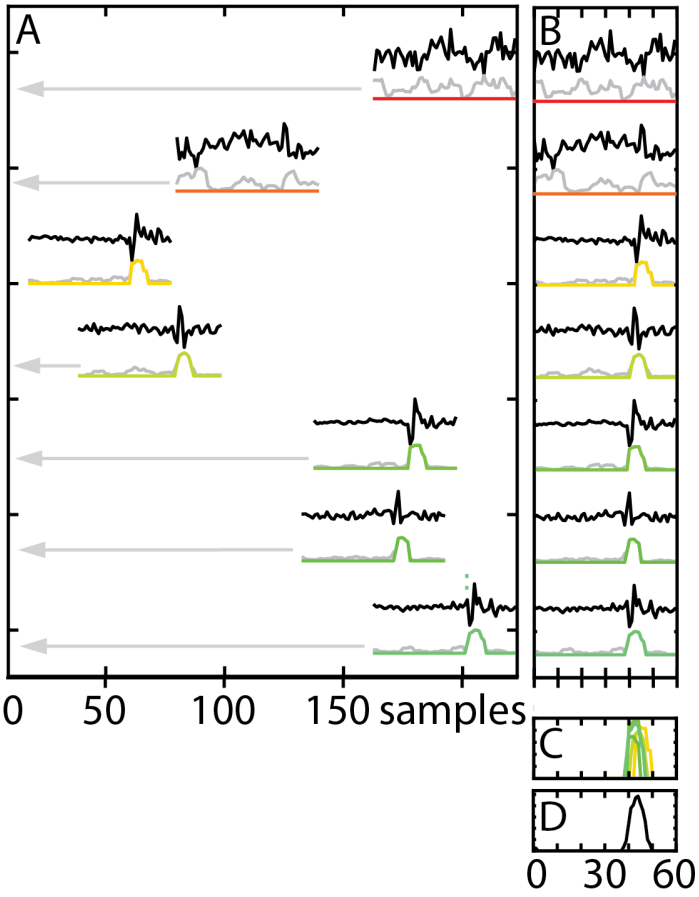

Figure S1: Example data processing for a single 0.24 second sub-window at a grid point containing a basal icequake. **A:** 1 Hz high-pass filtered horizontal component seismic data (black) from 7 seismic sites are converted to STA/LTA streams (light grey) and set to zero below an STA/LTA threshold of 3.2 (colored streams). Colors are used to allow distinguishable peaks in panel C but are otherwise not significant. **B:** STA/LTA data are then migrated backwards in time by the calculated travel time (shown by grey arrows in A) to the source grid point, where the peaks in STA/LTA line up. STA/LTA data are then weighted according to the horizontal distance between the seismometer and the grid point. **C:** Migrated and weighted STA/LTA data. **D:** Stacked STA/LTA data from all sites, showing a coherent peak. Data from 7 additional channels that contributed to this detection are omitted for clarity.

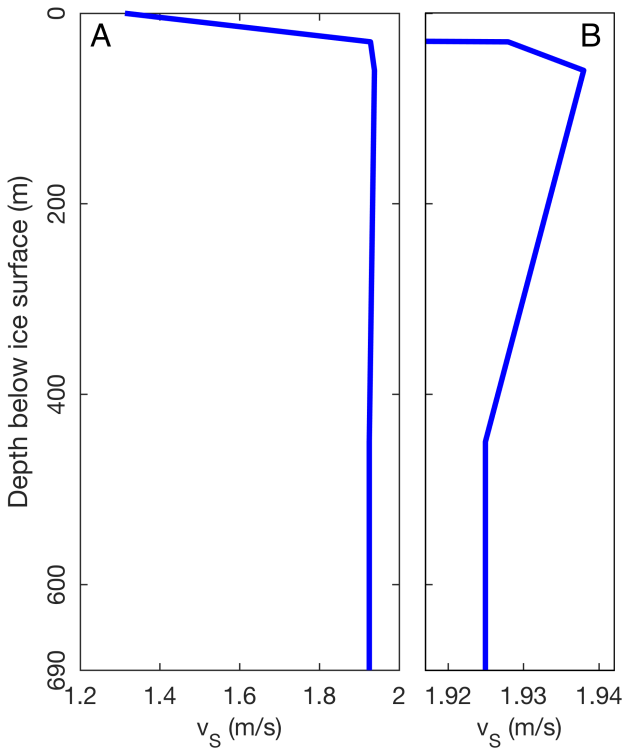

Figure S2: Ice S-wave velocity model used in backprojection. Panel **B** is a zoom of the right-hand-side of panel **A** over the same depth range.

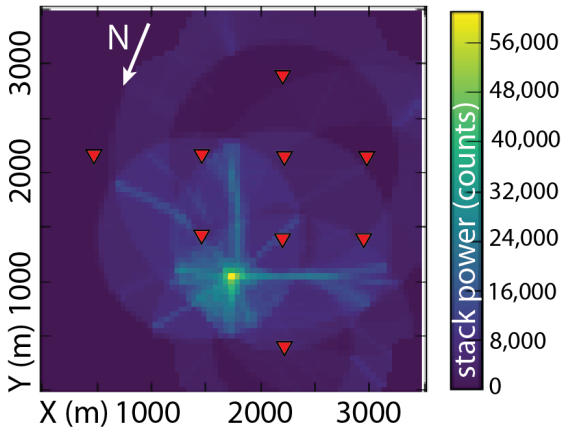

Figure S3: An example 'beam' generated for a single 0.24 second sub-window containing a basal icequake. Red triangles are seismometer locations in 2014, and grid point color is the power (sum of squared amplitude) of the stacked STA/LTA data (Fig S1D) at each grid point. The yellow grid point is where the stacked power is greatest for this 0.24 second sub-window and is the best location for this basal icequake. X- and Y-axes are in polar stereographic projection with origin at PS X = -229,500 and PS Y = -557,750 m.

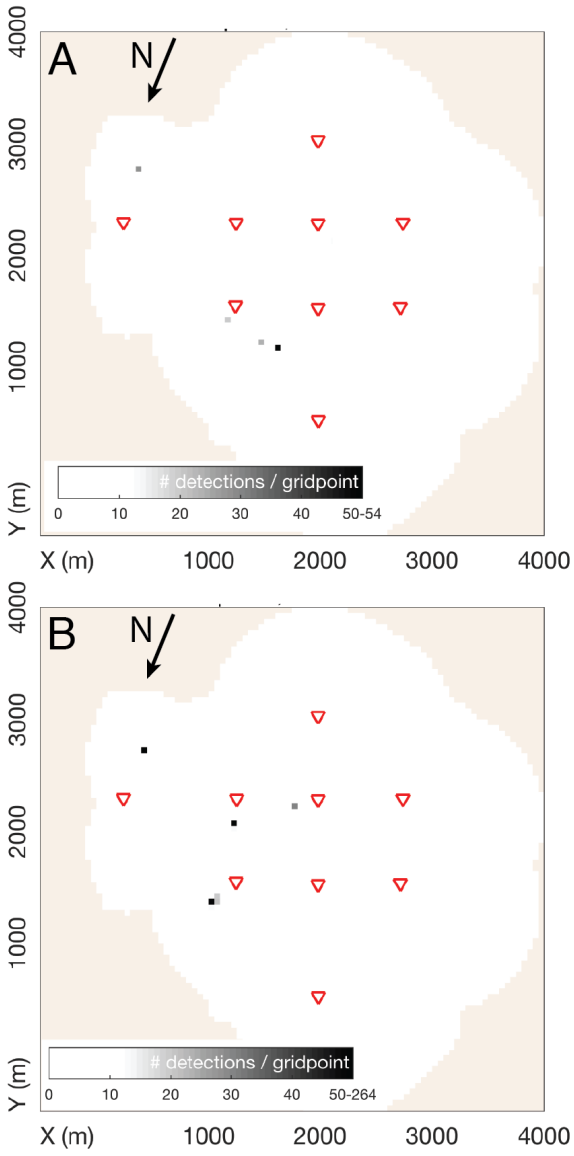

Figure S4: Number of icequakes detected per grid point by backprojection during two consecutive unstable slip events. **A:** Unstable slip event beginning Jan 8, 2014 16:30. **B:** Unstable slip event beginning Jan 9, 2014 08:55. **Both:** Red triangles are seismometer locations in 2014. Grid point color is the number of basal icequakes detected at that grid point for each unstable slip event. Grid point color is saturated at 50 basal earthquakes detected per gridpoint to highlight that basal icequakes only happen in a few locations beneath the seismic network in each unstable slip event. Note sparsity of detections. Tan represents the area outside of the

detection field, in which no basal icequakes can be detected because too few horizontal channels are available to trigger a detection. X- and Y-axes are in polar stereographic projection with origin at PS X = -229,500 and PS Y = -557,750 m.

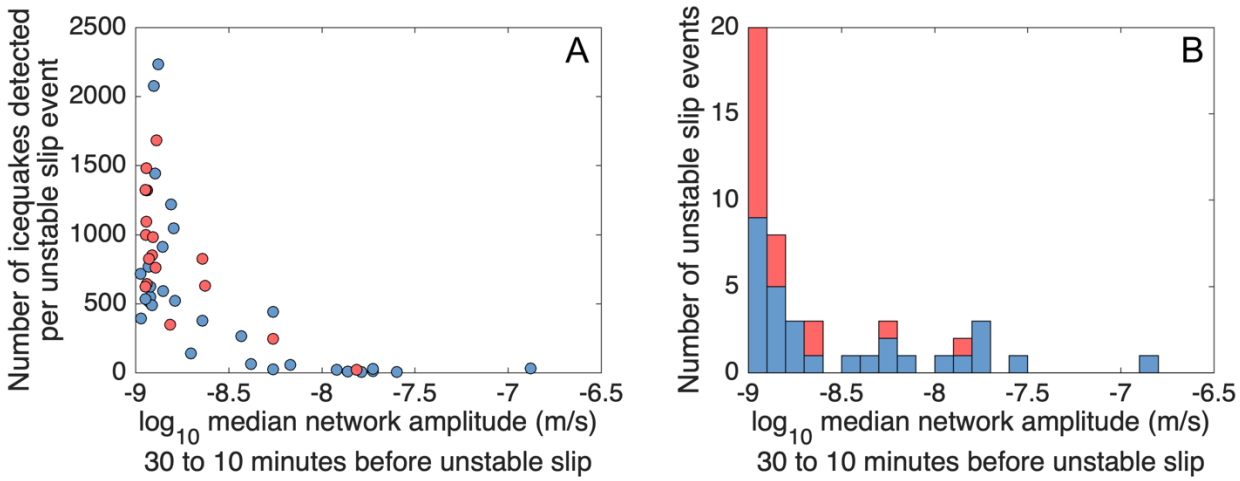

Figure S5: **A:** Comparison of basal icequake detection rates with seismic background noise levels. The total number of detected basal icequakes during each unstable slip event is plotted as a function of the median network seismic amplitude (m/s) of high quality 1-125 Hz bandpassed seismic data in the 30 to 10 minutes before each unstable slip event, before basal icequake activity begins. Note that individual unstable slip events may have variable numbers of basal icequake detections (100s-1000s) but slip events with very few detections also have the largest median network amplitude, or the highest background noise levels. **B:** Histogram of number of unstable slip events in each noise level bin, showing that most slip events have low noise levels. **Both**: Blue is unstable slip events from Jan-Feb 2014, and Red is unstable slip events from Jan 2015.

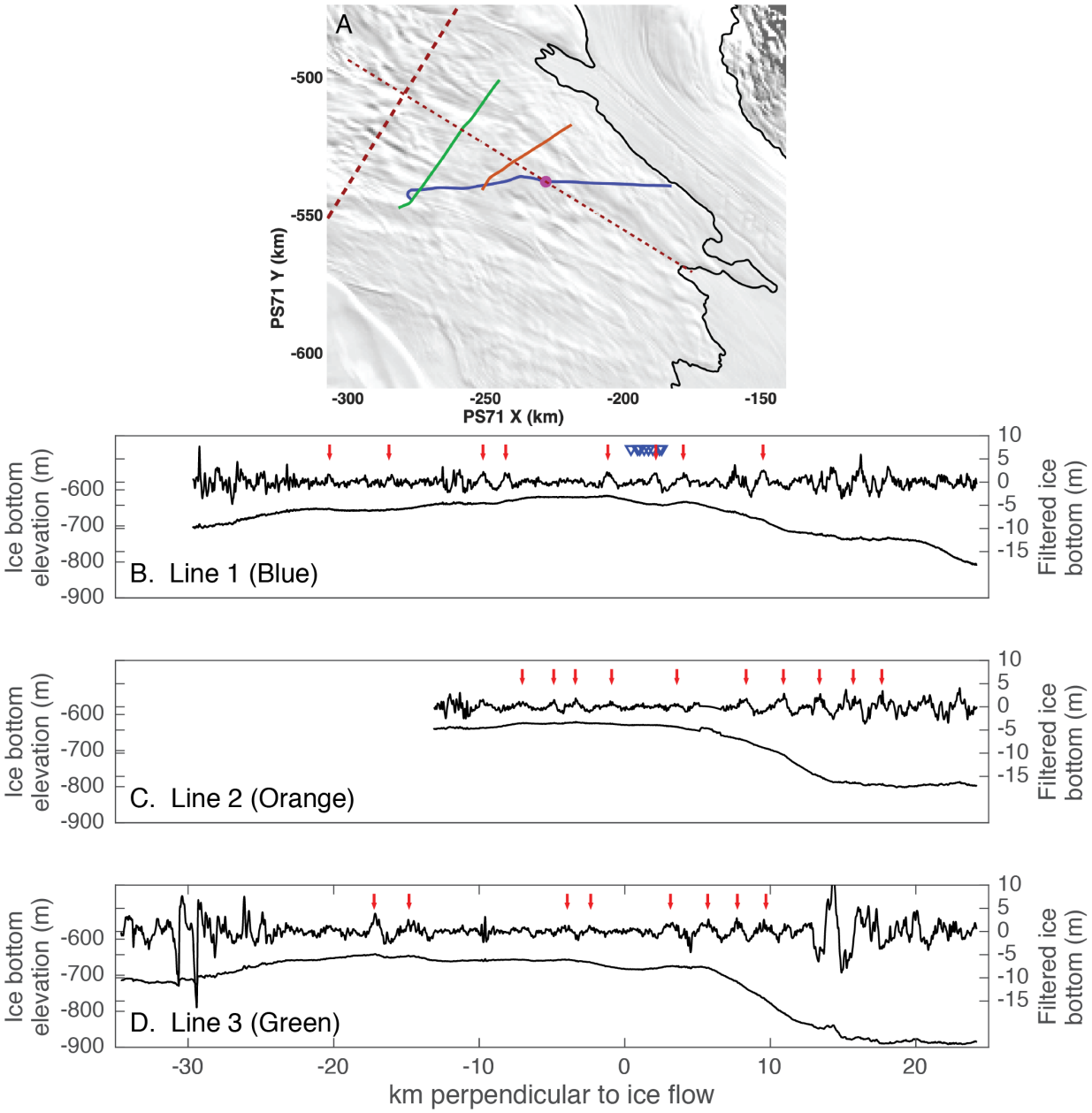

Figure S6: Three radar lines provide additional evidence of MSGL beneath the Whillans Ice Plain. **A:** Map of the WIP showing the three radar lines (blue, orange, and green lines), the location of the seismic network (magenta dot), the flow-vector determined from an on-ice GPS installed at the seismic network (thin dashed maroon line), and a line perpendicular to the flow vector (thick dashed maroon line). Black line is the grounding line from Bindschadler et al., 2011. PS X and Y positions for each radar line are rotated into an along- and across-flow

coordinate system using the GPS ice flow vector, and ice bottom elevation as a function of across-flow coordinate is plotted in **B, C, D**. In all three panels, the lower line is re-projected raw ice bottom elevation, and the top line is ice bottom elevation that has been resampled to 20 m spacing, detrended, and bandpass filtered between 100-3000 m. Red arrows point out low-amplitude basal topographic features that may be MSGL or other bedforms.